Mantle Phase Changes Detected from Stochastic Tomography

Vernon F. Cormier[1], Carolina Lithgow-Bertelloni[2], Lars Stixrude[2], and Yingcai Zheng[3]

[1]Department of Physics, University of Connecticut

[2]Department of Earth and Planetary Sciences, University of California, Los Angeles

[3]Department of Earth and Atmospheric Sciences, University of Houston

Corresponding author: Vernon Cormier (vernon.cormier@uconn.edu)

†Vernon F. Cormier, Department of Physics, University of Connecticut, 196A Auditorium Road, Storrs, CT 06269-3046

Index terms: 7208, 7203, 7260, 3611, 3612

Key Points:

- Stochastic tomography can capture higher order phase and chemical changes undetectable from reflection imaging.
- The heterogeneity spectrum of the upper mantle is marked by peaks associated with depth regions undergoing phase or compositional change.
- The upper mantle beneath the western US is consistent with a history of subduction and slab stagnation in the transition zone.

Abstract

Stochastic tomography, made possible by dense deployments of seismic sensors, is used to identify previously undetected and poorly detected changes in the composition and mineral structure of Earth's mantle. This technique inverts the spatial coherence of amplitudes and travel times of body waves to determine the depth and lateral dependence of the spatial spectrum of seismic velocity. The inverted spectrum is interpreted using predictions from the thermodynamic stability of different compositions and mineral phases as a function of temperature and pressure, in which the metamorphic temperature derivative of seismic velocities can be used as a proxy for the effects of heterogeneity induced in a region undergoing a phase change. Peaks in the temperature derivative of seismic velocity are found to closely match those found from applying stochastic tomography to elements of Earthscope and FLEX arrays. Within ± 12 km, peaks in the fluctuation of P velocity at 425, 500, and 600 km depth beneath the western US agree those predicted by a mechanical mixture of harzburgite and basalt in a cooler mantle transition zone. A smaller peak at 250 km depth may be associated with chemical heterogeneity induced by dehydration of subducted oceanic sediments, and a peak at 775 km depth with a phase change in subducted basalt. Non-detection of a predicted endothermic phase change near 660 km is consistent with its width being much less than 10 km. These interpretations of the heterogeneity spectrum are consistent with the known history of plate subduction beneath North America.

Plain Language Summary

Fluctuations in amplitude and traveltimes of seismic P waves from deep earthquakes observed at

the US Array of seismic stations are inverted for a depth dependent spectrum of the intensity of P wave velocity fluctuations. Peaks with depth of this spectrum correlate with the depths predicted for changes in the arrangements of atoms of the silicate minerals comprising the upper 1000 km of Earth's mantle. The structure of the peaks agrees with the known history of tectonic plate subduction beneath the western US.

1 Introduction

The best-known solid phase changes in Earth's silicate mantle are commonly detected from the reflection and conversion of body waves interacting with rapid, near discontinuous, changes in velocity and density occurring at or near 410 and 660 km depth (e.g., *Shearer*, 1991; *Niu et al.*, 2005). These phase changes also produce multi-pathed body waveforms between 15^0 -35^0 great circle range (e.g., Burdick and Helmberger, 1978; *Chu et al.*, 2012). The steepness of the inferred P and S velocity gradients between 410 and 660 km in reference Earth models, however, cannot be explained by plausible silicate mantle chemistry without the existence of at least one more phase change between 410 and 660 km. When the tools of mineral physics are applied to a constrained composition of the Earth's mantle, up to two additional phase changes are predicted to occur between the 410 to 660 km. Several other phase changes are also predicted above and below this zone, each having a unique behavior in their Clapeyron slope and the widths in depth over which each occurs (Fig. 1a). The widths of more than half of these are on the order of 15 to 60 km, making it difficult to detect them from reflected and converted body waves having similar or shorter wavelengths. A serendipitous seismological discovery from the inversion of P wave coherences across the USArray (Cormier et al., 2020) reveals that many these phase changes are marked by peaks in the depth-dependency of the mantle heterogeneity spectrum that correlate with peaks in the temperature derivatives of seismic velocities predicted by thermodynamic models of mantle composition and phase. Stixrude and Lithgow-Bertelloni

(2005 2007) have demonstrated that small lateral variations in temperature (<150^{o} K) allow the peaks in the predicted temperature derivatives to capture the depth zone in which two competing mineral phases my coexist that are capable of scattering seismic body waves (Fig.2). These peaks in the metamorphic component of the temperature derivatives can be used to identify and interpret peaks in narrow depth ranges of the mantle heterogeneity spectrum. This heterospectrum can be inverted from fluctuations in travel time and amplitudes of seismic waves observed across dense networks of seismic stations by a process known as stochastic tomography. In this paper, our objective is to interpret the seismological results from stochastic tomography applied to seismic arrays located in the western US (Cormier et al., 2020) using the predictions of the thermodynamic code Hefesto (Stixrude and Lithgow-Bertelloni, 2005, 2207) for the temperature derivatives of the P wave velocity. We assume mantle models of both equilibrium pyrolite and mechanical mixtures of harzburgite and basalt, and examine the effects of temperature and subduction. Before we begin interpretations in section 4, we review the principles and assumptions of stochastic tomography in section 2. In section 3 we discuss the filtering and depth averaging of the metamorphic temperature derivatives predicted by Hefesto required to match the sensitivity achievable with stochastic tomography. Readers primarily interested our interpretation of the detected phase changes may best begin by reading sections 4 and 5, which focus on the interpretation of our results, referring as needed, to the methods of inversion and analysis in sections 2 and 3.

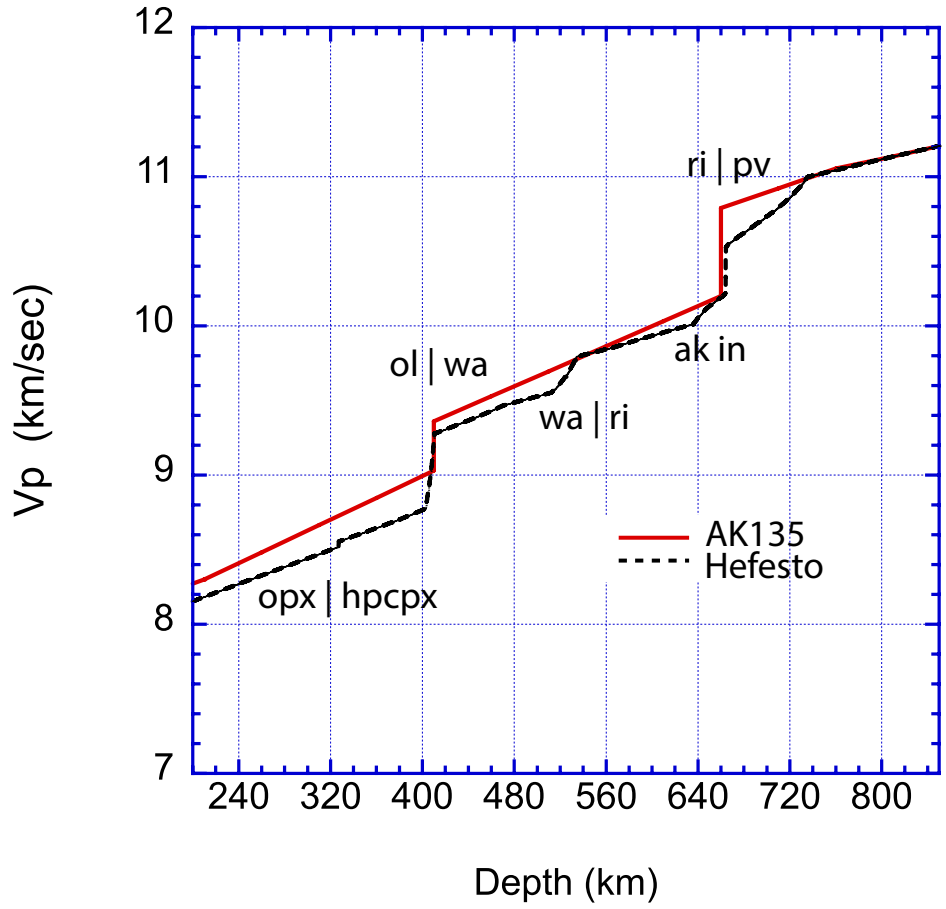

Figure 1. Dashed black line: P velocity of the upper mantle predicted by the thermodynamic modeling code Hefesto for a pyrolite composition along a 1600° K isentrope. Red solid line: P velocity of the AK135 model (Montagner and Kennett, 1995). Sharp, near vertical changes in slope occur for phase changes at 410 km and 660 km. Milder changes in slope predicted by Hefesto denote phase changes that occur over broader regions of depth. (Note: The generally slower Hefesto P velocities shown here, compared to a reference Earth model, are due to an average Earth geotherm cooler than the assumed 1600° K isentrope in the conductive zone near Earth's surface and cool perturbations due to slab stagnations in the transition zone (section 4).)

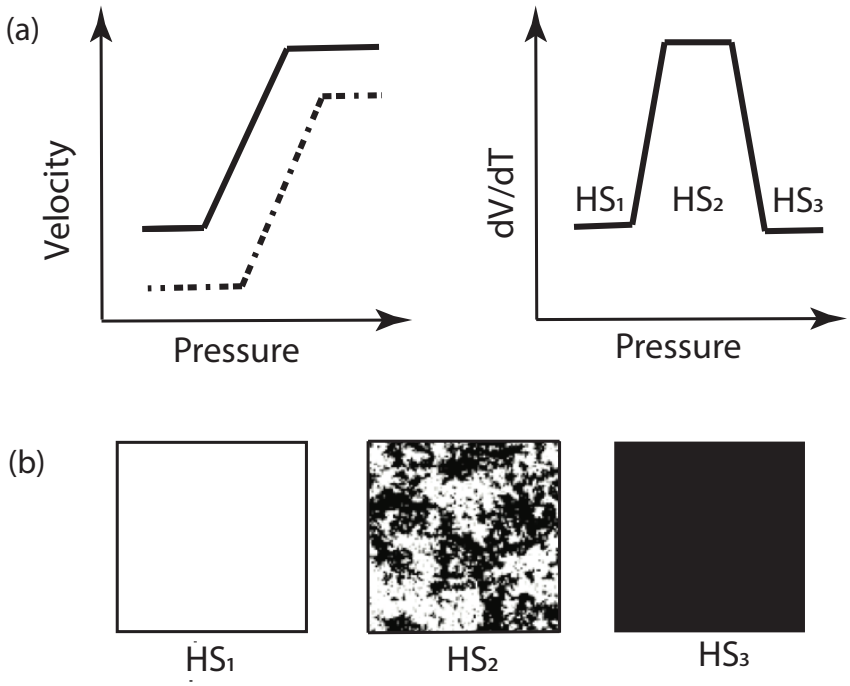

Figure 2. (a) Illustration of how a change in velocity over a zone of exothermic phase change affects its temperature derivative assuming a positive Clapeyron slope. Upper left: the solid line is the velocity change at lower temperature and the dotted line is the velocity change at higher temperature. Upper right: computed difference derivative of velocity with respect to temperature. (b) Realizations of the how the heterospectrm may change with depth across a phase change. The example shown here is inspired by Ising models of electron spin statistics for a ferromagnetic transition (Blundell and Blundell, 2014).

2 Stochastic Tomography

2.1 Theory and data

Small-scale heterogeneities, unresolvable by conventional tomography, have detectible signatures in the fluctuation of amplitudes and travel times observed across seismic arrays. Numerical simulations have shown that small-scale heterogeneity in the upper mantle can affect the wavefront of an incident teleseismic wave beneath an array. Small differences in the angle of approach of wavefronts, on the order of a several degrees or less, can produce unique signatures

in amplitude and phase fluctuations due to differences in the sensitivity of the wavefronts to the small-scale structure (e.g., Zheng & Wu 2008; Tkalčić et al., 2010). Measurement of these fluctuations between array elements can be exploited to invert for the spectrum of heterogeneity beneath the array with techniques that have been named stochastic tomography (Wu & Flatté, 1990; Wu & Xie, 1991, Zheng & Wu, 2008).

Transmission fluctuation coherence measurements (eqs. 1a-d) are the starting point for stochastic tomography. We consider the recorded fields due to two plane waves, PW1 and PW2. We use $U_1(x_1)$ for the recorded field at x_1 for PW1. Likewise, we use $U_2(x_2)$ for the recorded field at x_2 for PW2. Both fields propagate through the same heterogeneous medium. We also consider their corresponding reference fields (no heterogeneities), $U_{1ref}(x_1)$ and $U_{2ref}(x_2)$, respectively. We can write the seismic fields in amplitude and phase terms, for example, $U_1 = u_1 \exp[i\omega t] = u_1 \exp[i\phi]$ and $U_{1ref} = u_{1ref} \exp[i\omega t_{ref}] = u_{1ref} \exp[i\phi_{ref}]$. Similar representations are applied to PW2. A Rytov approximation provides the relationship between the scattered field and the reference field: $U_1 = U_{1ref} e^{\Psi_1}$. The complex function ψ has a real part, which is the logarithmic amplitude, and an imaginary part, which is the phase (or traveltime) difference with respect to the reference value. In our work, the observables are the ratios of log amplitude and travel time differences (eqs. 1c-d) from those computed in a reference Earth model. Transverse coherence functions are constructed as a function of the lag distance x between pairs of receivers. The brace brackets in eqs. 1a-b, define the logarithmic amplitude $\langle u_1 u_2 \rangle$ and $\langle \phi_1 \phi_2 \rangle$ phase coherences by averaging measurements for a specific lag distance over all combinations of two receivers in an array separated by that lag distance. Non-dimensional coherence values range from zero (amplitude and traveltime fluctuations) at neighboring receivers to 1 for perfect correlation of amplitudes and to 2π for perfect correlation of phase.

$$(1a) \qquad \langle u_1 u_2 \rangle = \frac{1}{2}\mathrm{Re}\langle \psi_1 \psi_2^* \rangle + \frac{1}{2}\mathrm{Re}\langle \psi_1 \psi_2 \rangle$$

$$(1b) \qquad \langle \phi_1 \phi_2 \rangle = \frac{1}{2}\mathrm{Re}\langle \psi_1 \psi_2^* \rangle - \frac{1}{2}\mathrm{Re}\langle \psi_1 \psi_2 \rangle, \qquad where$$

$$(1c) \qquad \psi(\omega) = \ln(u / u_{ref}) + i\omega(t - t_{ref})$$

$$(1d) \qquad u = \frac{\psi + \psi^*}{2} \quad and \quad \phi = \frac{\psi - \psi^*}{2\,i}$$

To construct the complex functions $\psi(\omega)$, we measure u and u_{ref} from observed and synthetic seismograms around the direct P waves from the outputs of a multi-taper filter at 0.7 Hz, and measure the traveltime difference $t - t_{ref}$ from cross-correlation of observed and predicted reference waveforms.

Stochastic tomography assumes that the functional behaviors of the coherences with lag distance are due to the interference of plane waves scattered by random heterogeneities having an unknown power spectrum as a function of wavenumber and depth. The transverse coherences can be written as an integral over horizontal wavenumber and depth, with an integrand containing the power spectrum (eqs. 2a-c).

$$(2a) \quad \langle u_1 u_2 \rangle = (2\pi)^{-1} \int_0^H d\xi a_1(\xi) a_2(\xi) \int_0^\infty J_0\left[(\kappa R(\xi)\right] \sin\left[\omega\theta_1(\xi)\right] \sin\left[\omega\theta_2(\xi)\right] P(\xi,\kappa)\kappa d\kappa$$

$$(2b) \quad \langle \phi_1 \phi_2 \rangle = (2\pi)^{-1} \int_0^H d\xi a_1(\xi) a_2(\xi) \int_0^\infty J_0\left[(\kappa R(\xi)\right] \cos\left[\omega\theta_1(\xi)\right] \cos\left[\omega\theta_2(\xi)\right] P(\xi,\kappa)\kappa d\kappa$$

$$(2c) \quad \langle u_1 \phi_2 \rangle = (2\pi)^{-1} \int_0^H d\xi a_1(\xi) a_2(\xi) \int_0^\infty J_0\left[(\kappa R(\xi)\right] \sin\left[\omega\theta_1(\xi)\right] \cos\left[\omega\theta_2(\xi)\right] P(\xi,\kappa)\kappa d\kappa$$

In eqs. 2a-c, P is the power spectrum as a function of depth ξ and horizontal wavenumber κ. H is the thickness of a heterogeneous layer. Functions a_1, a_2, θ_1, and θ_2 are defined in Cormier et al. (2020). The function R appearing in the argument of the Bessel function J_0 is the horizontal distance between the pair of rays arriving at a specific lag distance at depth ξ. The average sum of a coherence measurement at each lag from many sources at different distances and azimuths

159 can, in principle, be sensitive to the effects of scatterers whose size may be on the order of or less
160 than the spacing of array elements.
161
162 These integrals can be discretized and set-up as a linearized inverse problem in which the
163 squared difference of the observed coherences and predicted coherences of an unknown power
164 spectrum are minimized. The discretized forms of eqs.2a-c and the object function to be
165 minimized are given in Appendix B of Cormier et al. (2020).
166
167 The coherence data we chose to invert were 3 groups of deep focus earthquakes (Marianas,
168 Tonga-Kermedec, and South America) observed by elements of the US array, transportable
169 array, and FLEX arrays deployed in the western US (Fig. 3). Deep focus events were chosen to
170 avoid the effects of heterogeneity concentrated in the upper mantle near the source and to
171 eliminate the effects of near source reflections. P waveforms of 21,205 deep focus earthquakes
172 having moment magnitudes Mw 5.8-6.2 were downloaded from the Data Management Center of
173 IRIS. About 40% of these had sufficiently high signal to noise ratios and simple apparent
174 source-time functions to include in the coherence measurements. Within each earthquake group,
175 measured coherences are averaged at all receiver pairs corresponding to a specific lag.
176 Wavefront healing due to propagation from the source to the teleseismic receivers and averaging
177 coherences at each lag over all earthquakes aid in eliminating any source-side heterogeneity
178 effects. A joint inversion of data comprising 3 wavefronts arriving from widely different
179 azimuths, whose rays cross at variable depths beneath the array, makes it possible to achieve a
180 sensitivity to heterogeneity scales on the order of the smallest spacing (10 km) of array elements.

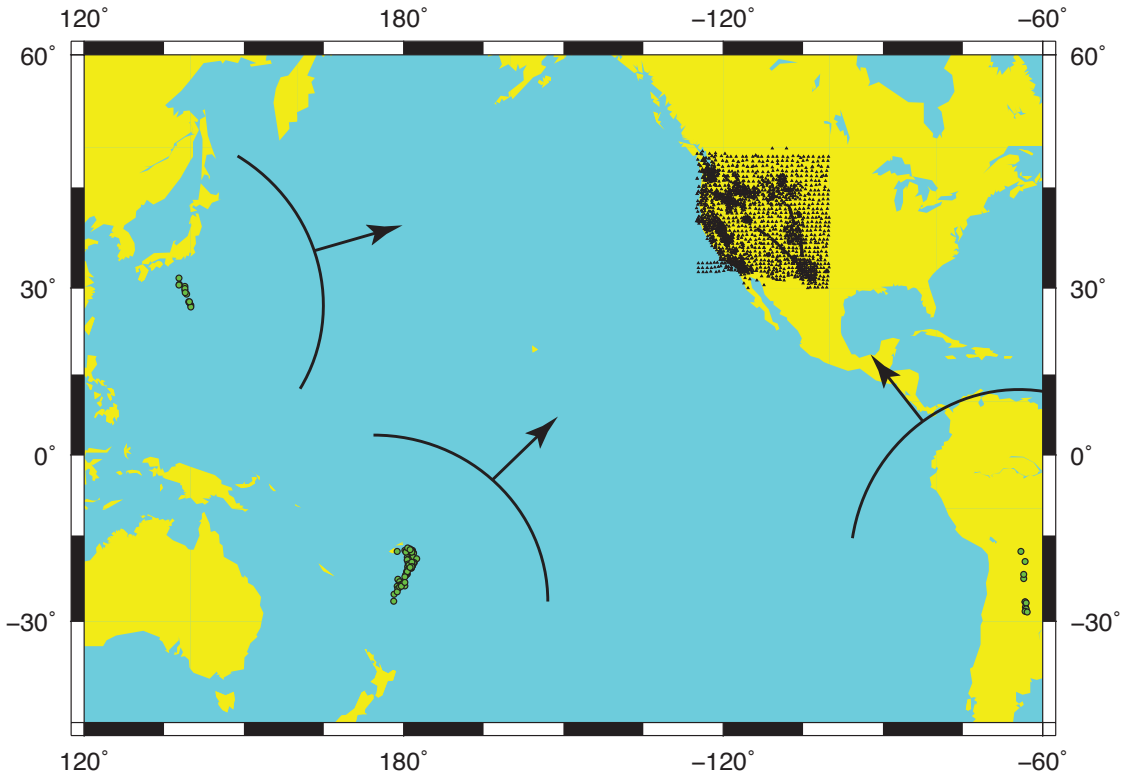

Figure 3. Hypocenters (green dots) of three deep-focus earthquake groups and US and FLEX Array seismic stations (black triangles) used in the inversion of P wave coherence for the upper mantle heterogeneity spectrum.

The inclusion of the effects of the specific earthquake source-time functions and radiation patterns in u_{ref} are essential to isolating the effects of forward scattering from those of the source. To achieve this for each event the reference synthetic seismogram u_{ref} at each array element was computed from the IRIS Syngine service (Nissen-Meyer, et al., 2014; https://service.iris.edu/irisws/syngine) in the AK135-F Earth model (Montagner & Kennett, 1995) using the known moment tensor solution for each event from the GCMT service (Ekstrom et al., 2012; https://www.globalcmt.org) and an empirical source time function determined by stacking P waves from each event in the 40° to 90° distance range. In conjunction with this paper we also provide a link to Python and Matlab scripts to assist researchers in designing experiments with stochastic tomography (Tian and Cormier, 2020). These example scripts treat

197 the effects of earthquake moment tensors and source-time functions on the reference wavefields
198 defining coherence measurements.

199

200 ### 2.2 Single layer inversion

201 As a first step it is useful to factor out the wavenumber dependence from a depth dependent
202 spectrum and compare its spectrum against published, non-depth dependent, stochastic models of
203 upper mantle heterogeneity. For understanding how lateral temperature differences drive mantle
204 heterogeneity such a comparison can also provide some constraints on the compositional and
205 temperature variations in the upper mantle. The coherence of broadband (0.02 to 2 Hz) body
206 waves can provide information at scale lengths intermediate between those estimated from global
207 travel-time tomography and the coda of higher-frequency body waves.

208

209 We thus first inverted for a uniform heterogeneity spectrum with depth in which the shape of the
210 power spectrum was defined by 4 parameters described in Cormier et al. (2020). To recognize
211 that the sensitivity of our coherence data peaked around a narrow band in wavenumber, we
212 employed a parameterization of the heterogeneity spectrum that consisted of a product of a low
213 pass and high pass filter in wavenumber (Klimes, 2002). Fig. 4a compares our inverted spectrum
214 for the upper 1000 km of the mantle to an overlapping band estimated by Mancinelli et al. (2016)
215 from scattered, low-frequency (<0.2 Hz), coda of teleseismic body waves. The two spectra
216 nearly coincide in a narrow wavenumber band centered near 0.065 km^{-1}. The dominant
217 frequency (0.7 Hz) of our P wave data in this wavenumber corresponds to a 100 km wavelength
218 in the upper mantle. At this center frequency, scattering will primarily be the Mie type in the
219 forward direction, with sensitivity strongest to heterogeneities having a scale between 10 to 100
220 km. A minimum detection threshold of 10 km scale agrees with the highest resolution
221 achievable by stochastic tomography with our smallest sensor spacings. It also agrees with our
222 detections and non-detections of phase changes predicted from thermodynamic modeling
223 (section 3).

224

225

226

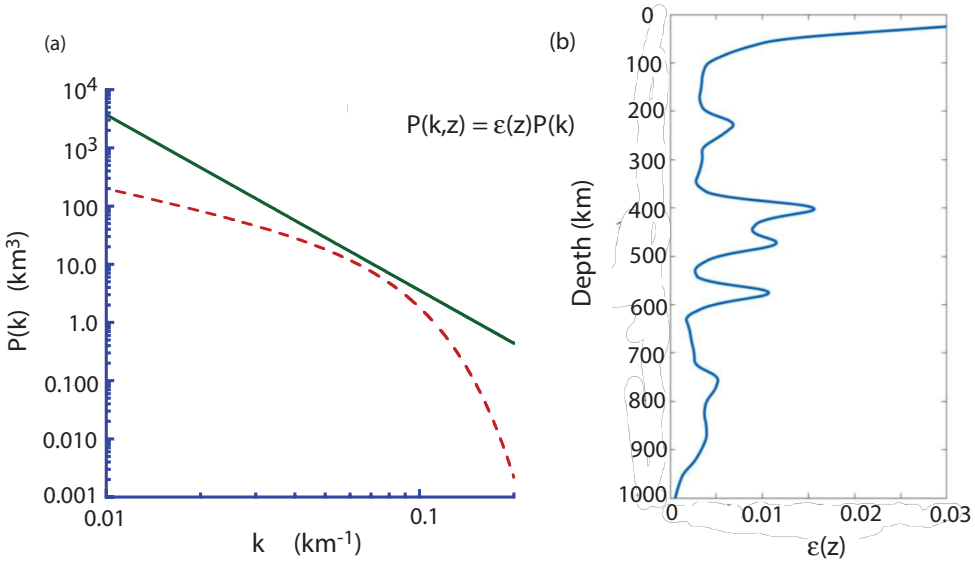

Figure 4. (a) Left: uniform power spectrum density of P velocity fluctuation for the upper 1000 km of Earth's mantle determined from stochastic tomography (dashed red line) compared to an overlapping portion of Mancinelli et al's (2016) estimates for this depth range in the frequency band of teleseismic body waves, (solid green line), in which Mancinelli et al.'s 1-D spectrum has been converted to a 3-D isotropic spectrum for a von Kármán medium using formulas in Sato et al. (2012). (b) Left: smoothed depth-dependent model of this spectrum determined from stochastic tomography applied to the mantle beneath the western US (Cormier et al., 2020).

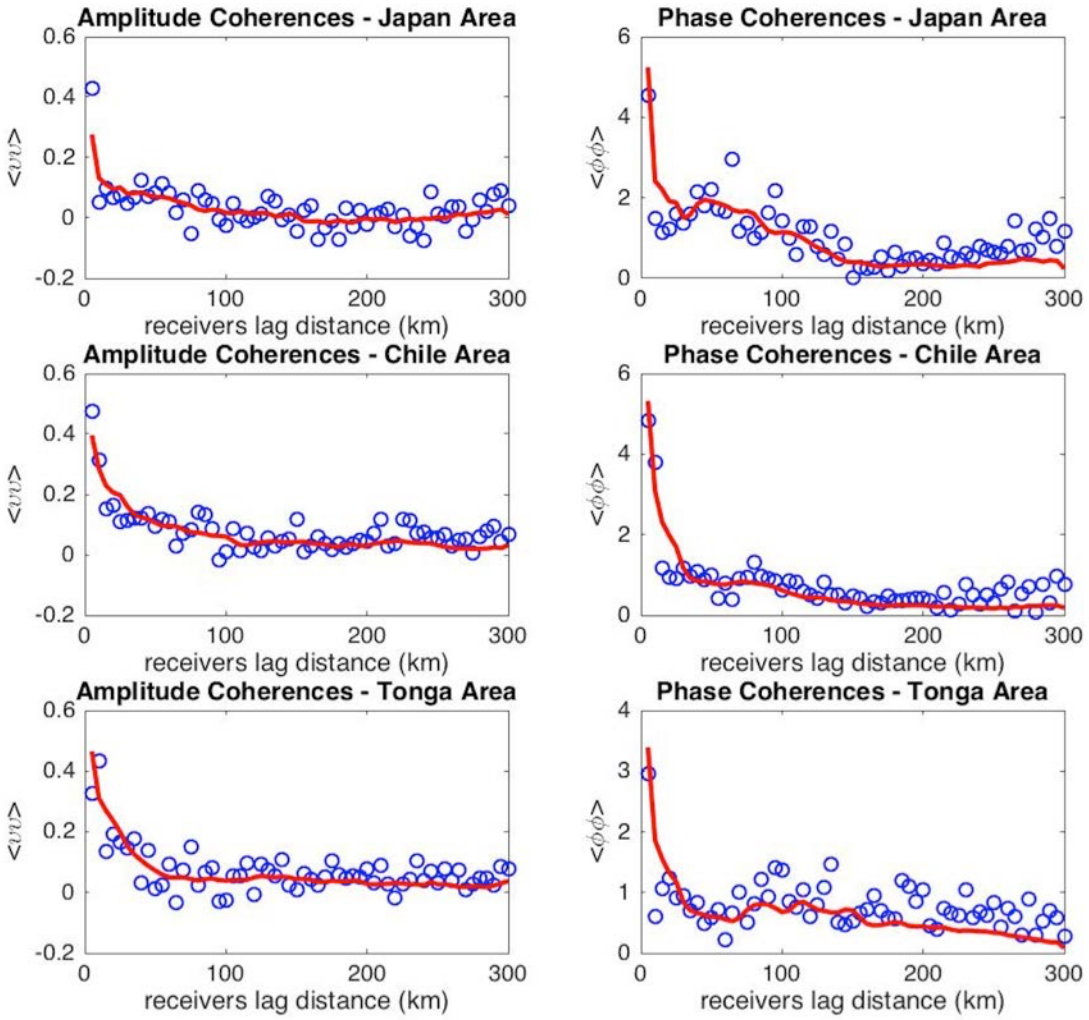

Figure 5. Observed coherences at all possible pairs of stations at specific lag distances (open circles) and predicted P wave coherence (solid lines) for a depth dependent model of mantle heterogeneity power (Fig. 4b) for the 3 epicentral regions shown in Fig. 3.

2.3 Depth dependent inversion

We next assumed that the spectral shape determined from the single layer inversion (Fig. 4a) was constant in depth but allowed its peak power to vary with depth in 40, 25 km thick, layers. Fig. 4b plots the inverted depth dependence of P velocity fluctuation. Fig. 5 compares the predicted coherences for the depth dependent model with the observed coherences for the 3 epicentral regions. Compared to the uniform model, the squared coefficient of determination of coherences for the depth dependent model increased from 0.74 to 0.80. The reduced χ^2

247 computed from observed and predicted coherences decreased from 1.65 to 1.05. The
248 significantly smaller, but not less than 1, χ^2 for the depth dependent spectrum is consistent with
249 an improved fit, but not an over-fit due to the assumption of a larger number of unknown
250 parameters. Interpretations of the depth dependent of model heterogeneity power are given in
251 section 4.

252 The 25 km thick depth intervals, which are close to the smallest sensor spacings (10 to 20 km) of
253 the denser FLEX arrays shown in Fig. 3, agree with the resolvable spatial scale determined in
254 sensitivity tests conducted by Wu and Xie (1991). In that study, Wu and Xie applied a stochastic
255 tomographic inversion to numerically synthesized seismograms in media having known depth-
256 dependent heterogeneity spectra in the presence of noise. For coherence inversions that
257 combined wavefronts arriving from different angles (e.g., Fig. 6), they found it possible to
258 achieve a depth resolution equal to the spacing of sensor elements.

259

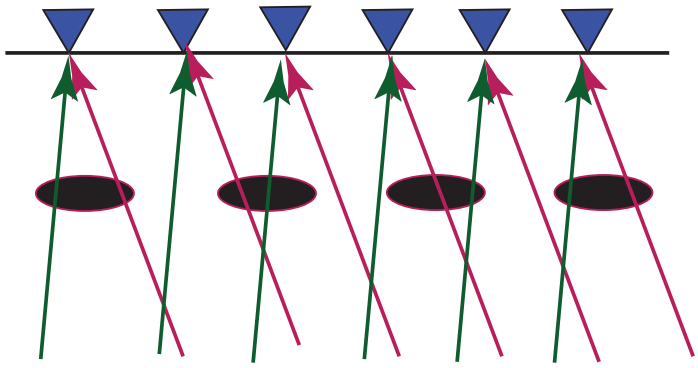

260 **Figure 6.** Illustration of how incorporation of wavefronts arriving from different directions (red
261 and green arrows) can enhance the resolution of small-scale heterogeneity (black ellipses).

262 **3. Hefesto: a thermodynamic model of mantle composition and phase**

263 3.1 Temperature derivatives of seismic velocity

264 Hefesto is a Fortran code for computing seismic velocities, densities, and other physical
265 properties for silicate minerals that minimize the Gibbs free energy at specific temperatures and
266 pressures (Stixrude and Lithgow-Bertelloni, 2005, 2007, 2022). Its input consists of pressure,
267 temperature, and a bulk composition in the SiO_2-MgO-FeO-Al_2O_3-CaO-Na_2O system, and

models of the properties of 51 end-members of 22 phases and their interactions. Among its output options are elastic velocities and density, as a function of depth. Isomorphic (constant phase) temperature derivatives of elastic velocity are calculated analytically but the additional contribution of a metamorphic component in the midst of a solid phase change can be calculated from difference derivatives determined by running the code at two closely spaced temperatures (e.g., Fig. 1a and Stixrude and Lithgow-Bertelloni, 2007). In the results shown in this paper, we calculated difference derivatives of, dlnVp/dT to double precision on a 64 bit processor, assuming either adiabatic or isothermal conditions, assuming two temperatures separated by 10^o K.

3.2 The metamorphic temperature derivative as a proxy for heterogeneity

Because the slope of the boundary between two stable silicate phases in P-T space is neither zero or infinite, any lateral change in temperature will also be associated with a change in the pressure (depth) of the phase boundary. This makes it possible for the temperature derivative of a to be used as a proxy for locating and measuring the width of a zone in which the two phases are competing for equilibrium (e.g, Fig. 2). Stixrude and Lithgow-Bertelloni (2007) have termed the temperature derivative of velocity in this situation the metamorphic derivative in recognition that its shape is affected by more than one form or phase of a mineral. The existence of two phases in the zone of the phase transition, with differing seismic velocities and density can scatter body waves. Hence, peaks in the predicted metamorphic component of the temperature derivative of a seismic velocity will be associated with peaks in the heterogeneity spectrum as a function of depth.

Implemented as a proxy for seismic velocity fluctuations, the values of dlnVp/dT require a conversion factor related to the mean lateral temperature variation to convert dlnVp/dT predictions to estimates of the mean fluctuations of P velocity, dVp/Vp. Stixrude and Lithgow-Bertelloini (2012) find that an upper bound of 150^o K for lateral temperature variations yield lateral velocity variations in agreement with seismic tomography in the upper mantle. Solomon (1976) also argues for 150^o K lateral temperature variations from geodynamic considerations. We apply a slightly more conservative estimate of 100^o K from comparing the scale of P velocity variations (order of 1 %) inferred from P travel time tomography to thermodynamic estimates of

297 the isomorphic temperature derivative (the temperature derivative not in a region of a phase
298 change). An alternative estimate of this conversion factor, not related to any assumption of
299 lateral temperature differences, is to estimate the maximum velocity fluctuation in a phase
300 transition zone between two competing phases. This is simply the difference in velocities
301 between two depth sides of a phase change divided by the average of the two velocities. For the
302 410 km phase change, this value is 3% from the Hefesto estimated velocity changes for both
303 pyrolite and harzburgite/basalt mixtures. This leads to the identical conversion factor of 150^{o} K
304 at 410 km. Given the existence of uncertainties in the lateral temperature differences and the
305 precise shape of the heterogeneity spectrum and its variation across the zone of a phase change,
306 we estimate that the true magnitude of P velocity fluctuations within most of the phase changes
307 occurring over zones wider than a wavelength is likely to lie between 1 to 3%.

308

309 3.3 Filtering for sensitivity compatible with stochastic tomography

310 A phase change that occurs over a depth range less than 6 km wide is unlikely to be detected as
311 narrow zone of increased heterogeneity that can be resolved by stochastic tomography applied to
312 sensor spacings between 10-20 km and coherence averaged over lag intervals 25 km and greater.
313 The 660 km phase change from ringwoodite to ferropericlase and magnesiowustie is estimated to
314 be 1-2 km wide in agreement with both other computational and experimental estimates in
315 mineral physics. Another phase change near 300 km depth from ortho-pyroxine to high pressure
316 clinopyroxene (opx to hcpx) is also quite narrow, Hefesto predicting it to occur over 8 km. Such
317 phase changes occurring over depth zones less than 10 km width are easily detected from
318 reflected and converted body waves. This is especially the case for 660 km phase change, which
319 has been observed in reflections at 1-2 Hz. The non-detection of the 660 km and 300 km phase
320 changes in our stochastic tomography inversions, sensitive to phase changes wider than 6 km, is
321 consistent with their narrowness. To compare Hefesto predictions with our stochastic
322 tomography inversions, we have hence applied a median filter to remove phase transitions less
323 than a body wavelength wide, and an averaging window nearly equal to observed coherence lag
324 intervals, to each point shown in comparison plots. This median filter, often used to remove
325 electronic spikes in seismic recordings (Evans, 1982), was designed to remove all signals in the

metatmorphic derivatives that are less than 6 km wide. Fig. 7 shows an example in which the median filter and averaging window has been applied to the Hefesto predicted temperature derivatives of P velocity.

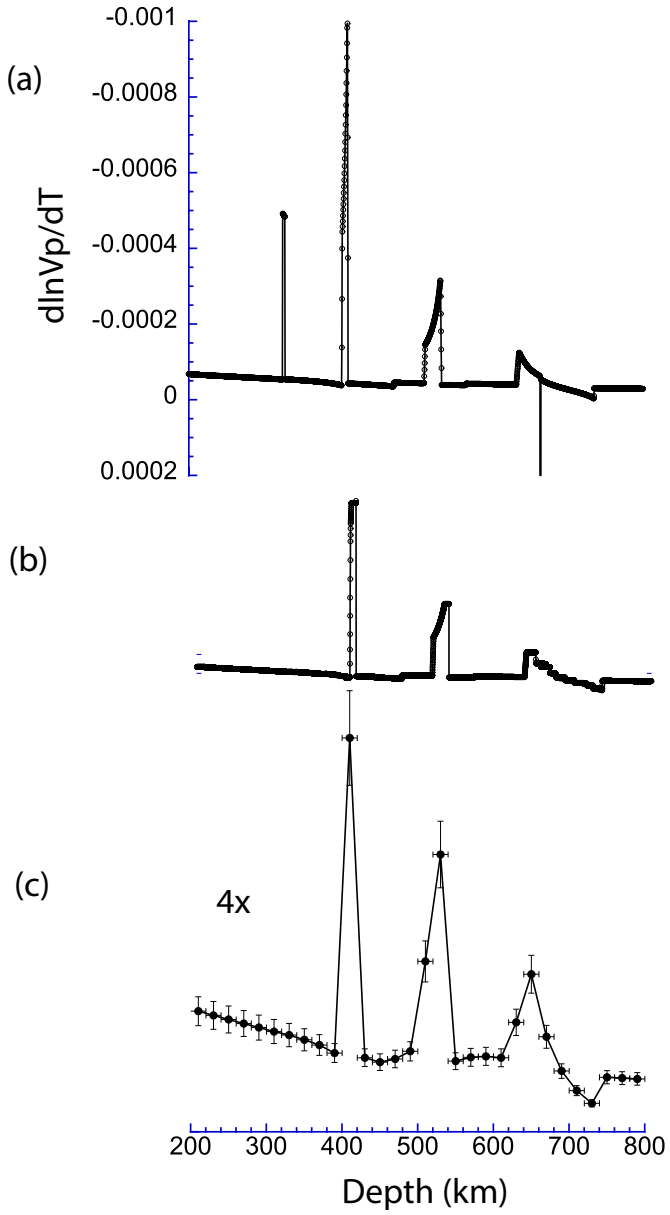

Figure 7. (a) Hefesto dlnVp/dT computed for a pyrolite model of the upper mantle; (b) followed by median filtering applied to (a) to remove signals less than 6 km wide; and (c) followed by 20 km wide depth averaging applied to (b).

333

334

335 **4 Results**

336 4.1 Interpretation of the depth dependent heterogeneity spectrum

337 Results of our inversion for a depth dependent heterogeneity spectrum for the upper 1000 km of
338 the mantle beneath the western US for the root-mean-square (rms) P velocity fluctuations are
339 shown in Fig. 8. These are compared with the Hefesto predictions for P velocity fluctuations
340 derived from the temperature derivatives of P velocity. The Hefesto predictions, for both an
341 equilibrium pyrolite composition (EA) and a mechanical mixture of harzburgite and basalt
342 (MM), are filtered and averaged to agree with the estimated sensitivities of stochastic
343 tomography (section 3). For the P velocity fluctuation predicted from stochastic tomography, the
344 horizontal uncertainty bars in depth in Fig. 8 are fixed at 25 km in length to represent the spacing
345 between averaged coherence lags, while maintaining a reduced chi-square greater than 1
346 calculated from predicted and observed coherences. For the P velocity fluctuations estimated
347 from Hefesto, the horizontal uncertainty bars are the width of a 20 km moving depth average of
348 the filtered temperature derivative of velocity. From numerical experiments recording the change
349 in the peak value of the predicted velocity fluctuation as the starting depth of the moving average
350 changes, the ordinate uncertainty bars are taken to be ±10% of the median peak value.
351

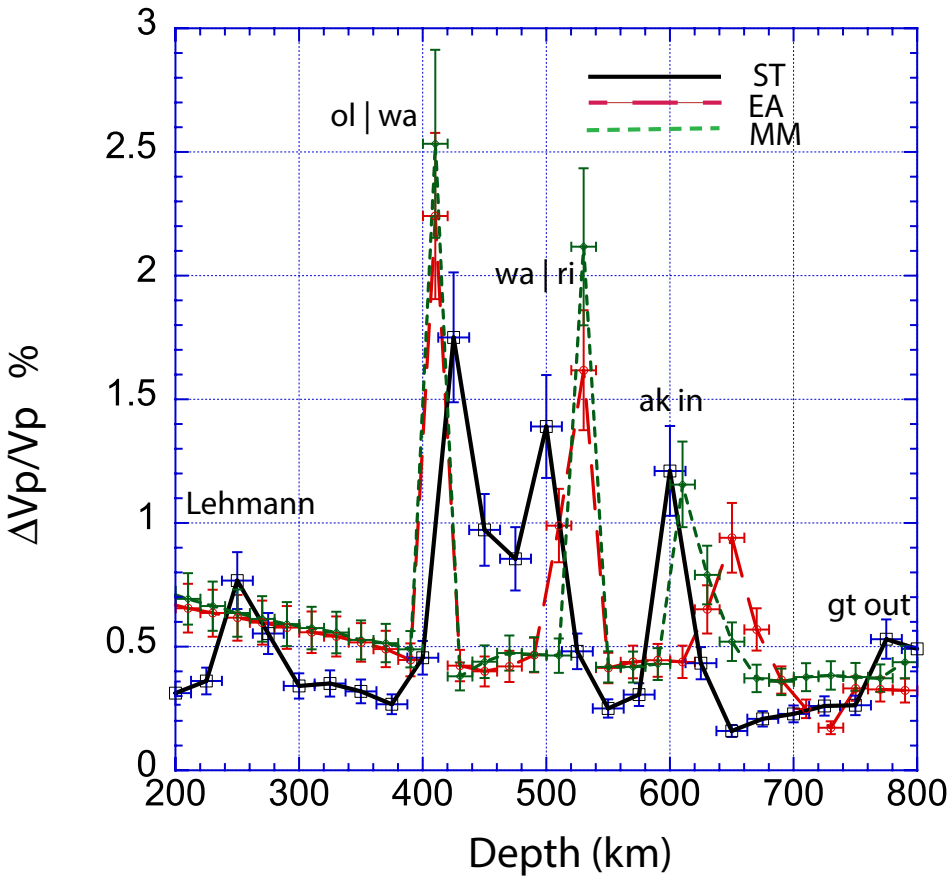

Figure 8. Solid black line (ST): the depth dependent heterogeneity spectrum for the rms fluctuation of P wave velocity in the upper 1000 km of the mantle estimated from stochastic tomography. Long dashed red line (EA): filtered temperature derivative of P velocity predicted for an equilibrium pyrolite model. Short dashed green line (MM): filtered temperature derivative of P velocity predicted for a mechanical mixture of 80% harzburgite and 20% basalt. Each thermodynamic prediction assumes an adiabatic temperature profile having a 1600° K. potential temperature. Interpreted detections of the Lehmann discontinuity and upper mantle mineral phase changes are labeled above or near peaks.

The Hefesto predicted peaks in the temperature derivative of seismic velocities are from metamorphic contributions due to changes in constituent mineral phases required to minimize Gibbs free energy. Runs are shown for an equilibrium pyrolite model and a mechanical mixture of harzburgite and basalt to simulate the effects of slab cycling. The expression of phase changes

367 can either be sharp or spread out over a depth range bounded by two changes in the gradient of
368 seismic velocity. If sharp (less than 10 km in width), the phase change can be easily detectable
369 from reflected, converted, or multi-pathed body waves. In these cases the effect of lateral
370 temperature variations will be expressed as topography on an apparent seismic reflector rather
371 than a zone of increased heterogeneity. The predicted phase change at 660 km of ringwoodite to
372 Mg-perovskite and magnesiowusite is one such example. Phase changes wider than 10 km in
373 depth may not be detectable in seismic reflections or receiver functions, but will be detectable
374 from stochastic tomography as a zone of discrete scatterers in a narrow range of depth close to
375 the width of a peak in the filtered Hefesto prediction for the temperature derivative of P velocity.
376 For these phase changes, the horizontal length scale of the scatterers will be related to the lateral
377 scale of temperature variations and the vertical scale to the width of the depth (pressure) range
378 over which the phase change occurs.
379
380 4.2 Largest peaks in the depth dependent heterogeneity spectrum
381 The depths and relative amplitudes of at least three of the peaks in the heterogeneity spectrum
382 measured by stochastic tomography agree well enough with those predicted by Hefesto to have
383 confidence in an identification of the detected phase change. These are:
384
385 (1) a peak at 425 ±12 km depth nearly matches a Hefesto predicted phase change of olivine
386 to wadsleyite (ol | wa) at 412 km occurring over a 10 km width;
387 (2) a peak at 500 ±12 km depth matches a Hefesto predicted phase change of wadsleyite to
388 ringwoodite (wa | ri) at 500 km occurring over 20 km width;
389 (3) in mechanical mixtures of harzburgite and basalt (MM), a peak at 600 ±12 km matches
390 the interference of two predicted phase changes, each exothermic with positive
391 temperature derivatives of velocity. Together they occur over a 30 km width. In
392 equilibrium pyrolite, these phase changes are predicted to be deeper at 640 km depth.
393
394 At 600 km depth the predicted signal in the temperature derivative of velocity consists of a
395 relatively wide peak in which the shallower wadsleyite to ringwoodite phase change
396 interferes with an initiation of a deeper calcium perovskite phase (capv in). The 600 km
397 initiation of akimotoite is not the deeper endothermic phase change associated with the

sharp discontinuity commonly detected near 660 km. For some compositions and temperatures, Hefesto predicts the 660 km phase change to occur over two sharp, and closely spaced depths. These two deeper phase changes are too sharp to be detected by stochastic tomographic with the array and frequency band of this study. Both seismic observations and mineral physics studies (e.g., Ishii et al., 2001), predict a 660 km deep phase change to occur over a zone equal to or less than 2 km. In the median filtered Hefesto predictions shown in Figs. 7c and 8 the phase changes near 660 km vanish, but appear in the unfiltered Hefesto prediction shown in Fig 7a.

If our estimated error bars in depth are close to truth, the 600 km phase change detected from stochastic tomography favors a harzburgite rather than a pyrolite composition in the mantle transition zone. Within error bars, our stochastic tomography detection at 500 km depth for the wadsleyite to ringwoodite phase change is shallower than either the Hefesto predictions for either pyrolite or a mechanical mixture. The disagreement is similar for both compositional models, suggesting that a better agreement may be achieved either by revising the Hefesto inputs for the physical properties of individual minerals or by revising the temperature profile. Of these two inputs, the depth of phase changes is most strongly sensitive to the temperature profile. In section 5, we discuss how a negative temperature perturbation in the 410 to 660 km transition zone, consistent with a history of subduction, can bring the observed and predicted heterogeneity spectra into closer agreement.

4. 3 Smaller peaks in the depth dependent heterogeneity spectrum

4.3.1 775 km

Another peak requiring a small negative perturbation to an assumed adiabatic temperature profile having a 1600 deg K potential temperature is a peak at 775 ±12 km. This peak nearly correlates with a Hefesto predicted phase change at 795 km in mechanical mixtures of basalt and harzburgite having a basalt fraction of 18%, indicative of a phase change in subducted oceanic crust. The Hefesto predicted phase change in the temperature derivative consists of relatively weak peak having a 7 km width.

4.3.2 250 km

The heterogeneity peak at 250 km ±12 km is neither the orthopyroxene to high pressure clinopyroxene phase change predicted closer to 300 km or the X discontinuity found in many receiver function studies (Pugh, 2021), both of which are too narrow (<10 km) to be detected by stochastic tomography and the filtered Hefesto predictions shown in Figs. 7bc and 8. We instead interpret this to be a signal associated with the Lehmann discontinuity, which is frequently detected in S body wave studies at depths 220 km to 240 km beneath continents (e.g., Vinnik et al., 2015). Karato (1992) has suggested that the Lehmann discontinuity is associated with a change in rheology from dislocation creep above to diffusion creep below a 20 km wide or greater zone centered near 240 km depth for wet and/or hot conditions. This transition is also associated with a change from an anisotropic lithospheric lid to an isotropic asthenosphere. A change in anisotropy and rheology, however, is unlikely to be strongly expressed by a zone of heterogeneity capable of scattering seismic waves. Vinnik et al. (2005) have also shown that a change in rheology and anisotropy alone cannot account for the sign of the S to P conversion of S waves incident on the Lehmann discontinuity. A possible mechanism for heterogeneity in this depth region may be the hypothesis of Ono (2007), who proposes that the Lehmann is due to the effects of dehydration of subducted oceanic sediments beneath a continent. A possible supporting piece of evidence for this hypothesis is that Hefesto does not yet include the effects of H_2O content on melting and dehydration.

4.4 Modeling considerations: resolution and temperature profile

The differences between detected and predicted phase changes will depend on the accuracy of the assumptions in the thermodynamic model and the sampling and errors in the power spectrum of heterogeneity determined from stochastic tomography. The depth accuracy of the thermodynamic model depends on the validity of the assumed petrologic model, the physical properties of minerals determined from combinations of experimental observations and ab initio calculations, and the assumed temperature profile. The accuracy of the power spectrum estimated from stochastic tomography largely depends on the depth-sampling rate that can be resolved in the inversion of coherences, which depends on sensor spacing and its geometry and the azimuthal and depth distribution of seismic events.

459 The disagreement between the detected (600 km) and predicted (660 km), last and deepest,
460 endothermic phase change is too large to be explained by a plausible hotter mantle temperature
461 in this broad region. A global 660 km discontinuity has been largely confirmed in many seismic
462 studies and is generally the most robustly detected discontinuity even by reflected body waves
463 having dominant frequencies approaching 1 Hz (e.g., Deuss et al., 2006). Its signature in
464 receiver functions (Andrews & Deuss, 2008), however, can be complex, in agreement with the
465 complex phase changes predicted from thermodynamic models at and near this depth (Xu et al.,
466 2008). A partial explanation for a positive detection at 600 km but not 660 km is that the 25 km
467 sampling rate in the inversion is simply too coarse to resolve the complex signal of two closely
468 spaced phase changes. We thus conclude that our detection at 600 km is the transformation of
469 high-pressure clinopyroxene to akimotoite initiating closer to 600 km than 650 km. Hao et al.
470 (2019) predict this transition to have a width on the order of 25 km or greater. The detection of
471 an akimototite transition at 600 km, indicative of the existence of regions of colder mantle
472 temperatures (Hogrefe et al., 1994), coupled with a phase transition in basalt at 775 km, is
473 consistent with the history of the subduction of the Farallon plate beneath the western US.
474 Tomographic images of the shear velocity structure of the mantle beneath this region reveal
475 evidence of both slab stagnation and fragmentation in the lower mantle transition zone as well as
476 penetration beneath 660 km (Schmid et al., 2002).
477
478
479 ### 4.5 Geotherm perturbation

480 Two isothermal runs of Hefesto (Fig. 9) demonstrate the relative sensitivity of different predicted
481 phase transition to changes in temperature. The 410 and 660 km phase transitions are
482 considerably less sensitive to lateral temperature variations than the calcium perovskite and
483 akimotoite transitions near 500 and 600 km depth, respectively. Hence, if the physical properties
484 and chemistry of these two transitions are well understood, they can potentially serve as accurate
485 thermometers in the transition zone. Assuming that errors in of the chemistry and physical
486 properties taken as inputs to Hefesto are small, we can estimate the temperature required to make

the transition zone phase changes come into better agreement with our measurements of heterogeneity in the transition zone from stochastic tomography. The perturbation needed to achieve this (Fig. 10) requires a cooler transition zone temperature compared to that calculated for a mantle adiabat having a 1600^{o} K potential temperature. It is also worth noting that the negative temperature perturbation required to bring the akimotoite phase transition at 600 km into better agreement with a pyrolite model may not require as high a percentage of harzburgite in models having a mechanical mixture (Zhao, et al., 2022). An example applying this temperature perturbation is shown in Fig. 11. The size and form of this perturbation is similar to those proposed in mantle convection studies by Tackley (1993) and Matyska and Yuen (2002), who predict non-adiabatic perturbations to the mantle geotherm due to slab stagnation in the transition zone. In addition to the results shown here from stochastic tomography, travel time tomography also supports this condition for the subduction of the Farallon slab beneath the western US. East-west cross sections of the P wave tomographic model LLN3D are consistent with a fast, cool, region in the mantle transition zone (Fig. 12).

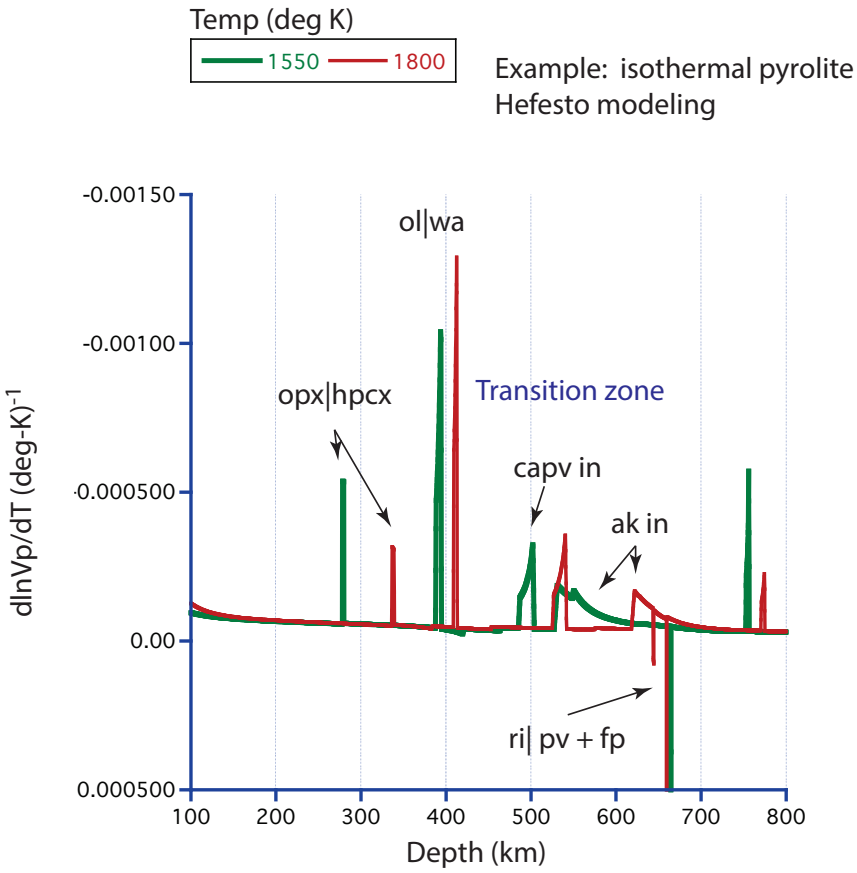

501

502 **Figure 9.** Isothermal calculations of dlnVp/dT for pyrolite for 1600° K. and 1800° K.

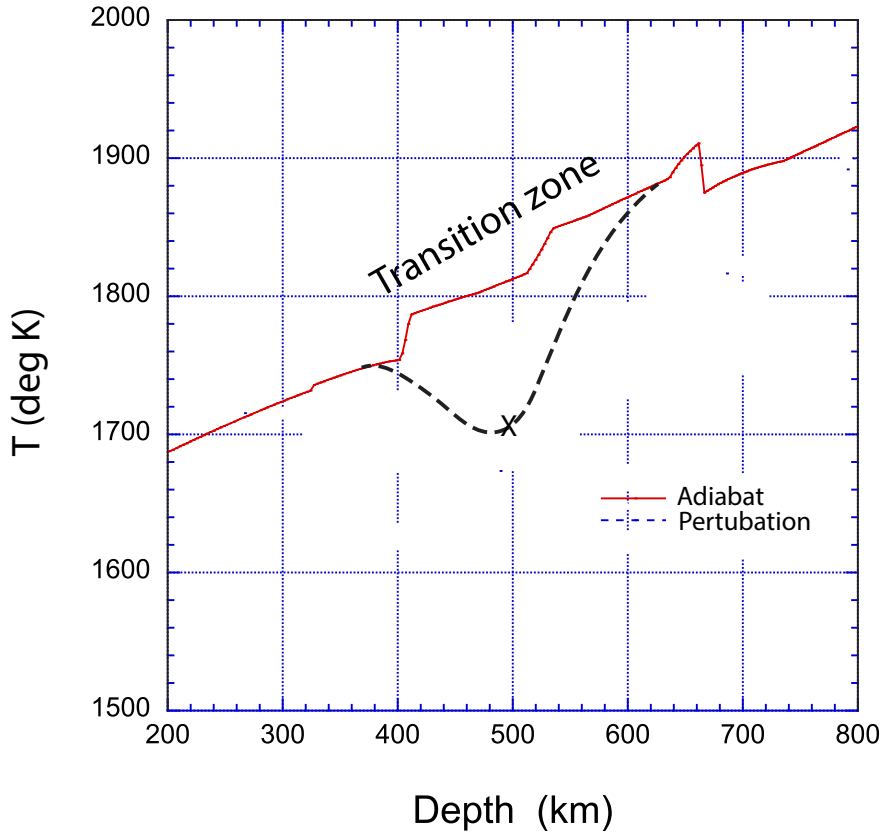

503

504 **Figure 10**. A perturbation (dashed) is applied in an adiabatic temperature profile in the
505 transition zone to achieve better agreement between the peaks in heterogeneity determined from
506 stochastic tomography and those predicted by the Hefesto thermodynamic code. The X marks the
507 temperature perturbation needed to make depth of the wadsleyite to ringwoodite phase transition
508 predicted from an isothermal run of Hefesto agree with the 500 km deep peak found from
509 stochastic tomography.

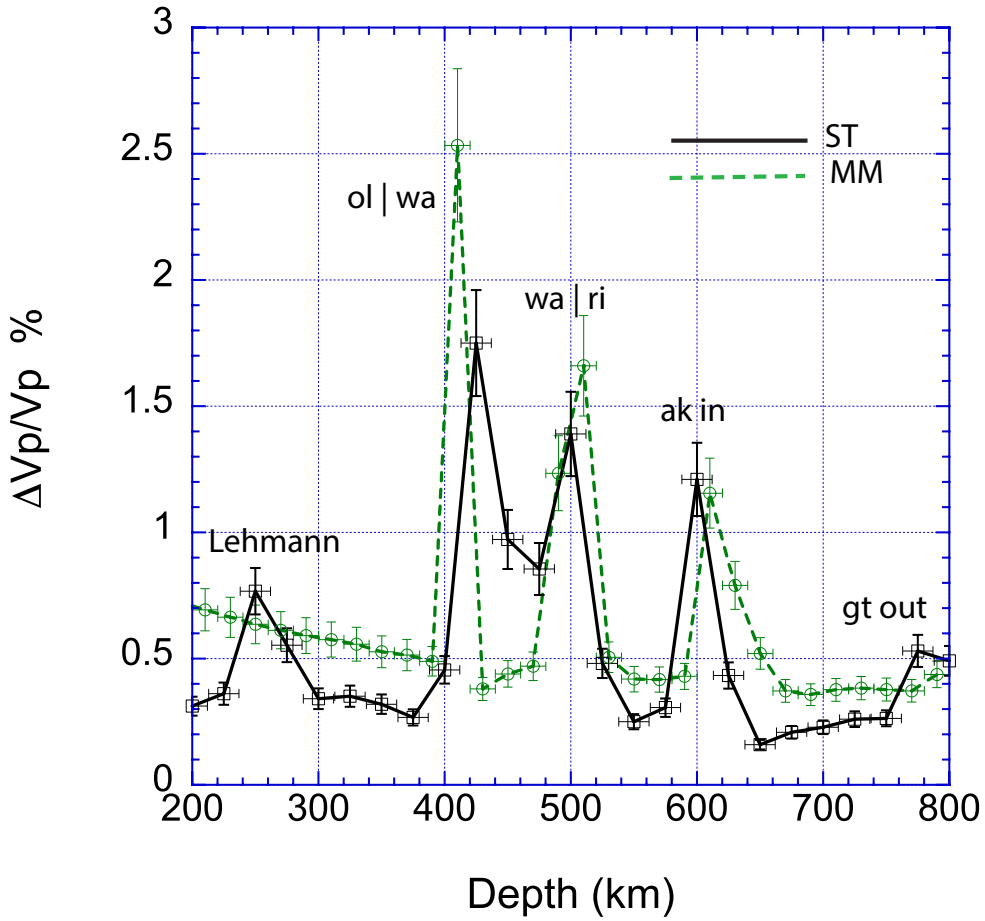

510

511 **Figure 11**. Solid black line (ST): mantle heterogeneity spectrum of P waves measured from
512 stochastic tomography applied to the western US. Short green dashed line (MM): temperature
513 derivative calculated from the Hefesto thermodynamic code for a mechanical mixture of
514 harzburgite and basalt assuming the temperature perturbation in the transition zone shown in
515 Figure 10.

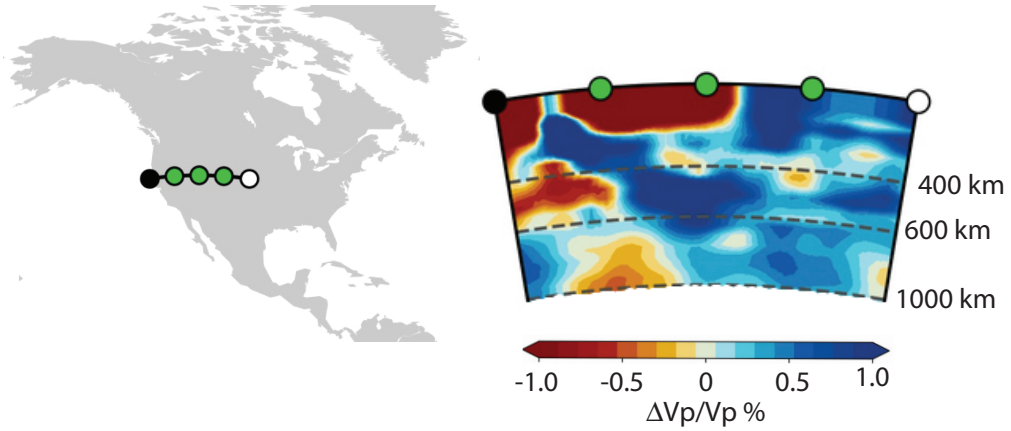

516

517 **Figure 12.** Cross-section of P velocity structure beneath the western US along an E-W profile
518 centered at 50 deg latitude from the LLN3D model of Simmons et al. (2012, constructed from
519 SubMachine web tools (Hosseini et al., 2018).

520 The combination of mechanisms creating slab stagnation are still actively debated, depending on
521 slab rollback at the initial subduction zone, the fine structure of the endothermic phase change
522 near 660 km, its Clapeyron slope, and whether there is a viscosity increase or decrease below the
523 660 km phase change (e.g., Mao and Zhong, 2008). The non-detection of 660 km phase change
524 from stochastic tomography, its otherwise ubiquitous detection from reflected and converted
525 high frequency (> 1 Hz) body waves (e.g., Whitcomb and Anderson, 1970), the narrow width of
526 metamorphic temperature derivatives of its P and S wave velocity changes, and its topography
527 are all consistent with it being an endothermic phase change, very narrow in width (no more than
528 2-10 km), with a near vertical Clapeyron slope.

529

530

531

532 # 5 Conclusions

533 From stochastic seismic tomography applied to the upper 1000 km of the western US, we have
534 shown that its heterogeneity spectrum is characterized by a series of peaks related to narrow
535 regions of depth in which phase or chemistry changes. We have demonstrated the stochastic
536 seismic tomography can capture higher order phase and chemical changes in the upper mantle
537 that are undetectable from reflection imaging. These peaks, having amplitudes on the order of 1-
538 2% in P velocity fluctuation, strongly correlate with the majority of predicted phase changes
539 from thermodynamic models of the upper mantle's chemistry and phase. Stochastic tomography
540 has the potential to detect mantle phase changes that do not exhibit changes in seismic velocity
541 and density over short depth intervals. These types of phase changes are characterized by paired
542 changes in velocity gradient over a transition depth that may be equal to or larger than the
543 wavelength of a body wave. Results from a depth-sampling interval of 25 km for the inverted
544 spectrum suggest that many of these phase changes may occur over a range in depth equal to or
545 greater than 25 km. An exception is our non-detection of the phase transition at 660 km,
546 consistent with a transition interval in depth that may be as small as 2 km (0.1 GPa).
547
548 Our interpretation of individual peaks in the heterogeneity spectrum as a function of depth are
549 consistent with a history of subduction and slab stagnation in the upper mantle transition zone
550 between 400 to 660 km depth. This interpretation is based largely on the depth position and
551 temperature dependence of the detected wadsleyite to ringwoodite transition at 500 km depth and
552 the calcium perovskite to ringwoodite transition at 600 km depth. A stochastic tomography
553 detection of a smaller phase transition near 250 km is interpreted to be the Lehmann
554 discontinuity, which is unpredicted by thermodynamic modeling not containing effects of water,
555 and which may be the signature of dehydration of subducted oceanic sediments. The depths of
556 the 500 km, 600 km, and a 775 km phase change require a negative perturbation of a mantle
557 adiabat in the transition zone, extending at least 100 km below the 660 km phase transition. This
558 cool perturbation is consistent with the predictions of mantle convection suggesting slab
559 stagnation in the transition zone, with the predictions of thermodynamic modeling incorporating

perturbations to the geotherm, and with fast P velocities in the mantle transition zone found in 3-D travel time tomography of the western US.

To detect the thermodynamically predicted changes in mantle silicates with stochastic tomography, we demonstrate that a depth sampling interval of 25 km or less must be achieved. Such a resolution may generally also require an estimation of the amplitude and phase effects of source radiation patterns and source-time functions. Averaging of coherence lags over all pairs of sensors having a common lag distance over a large number of earthquakes arriving from different azimuths will enable heterogeneities having scale lengths on the order of the sensor spacing to be detected and will also tend minimize site effects at the near surface of sensors. The 10-20 km spacing of a growing number of FLEX array experiments of the US Array and the availability of waveforms from 3 widely separated groups of deep focus earthquakes, having simple source-time functions, makes this high resolution possible for at least the western US. Our location of phase changes represents an average for the western US for depths between 200 km and 1000 km, between latitudes 30^{o} N and 50^{o} N and longitudes 100^{o} W and 125^{o} W. Quantification of lateral variations in these phase changes over smaller regions of the upper mantle will depend on the densities and duration of FLEX array experiments and the availability of body wavefronts arriving from different azimuths.

Acknowledgments and Data

This study incorporated work initially funded by the National Science Foundation under grant EAR 14-46509 (Vernon Cormier) and grant EAR 16-21878 (Yingcai Zheng). Figure 3 was drawn using the Generic Mapping Tools (Wessel and Smith, 1998).

Waveform data and services for centroid moment tensors and synthetic seismograms are available from the Incorporated Research Institutions for Seismology through the web site https://www.iris.edu. Matlab and Python scripts for processing and inverting amplitude and phase coherences for single layer and depth dependent heterogeneity spectra are available from the web site listed in the Tian & Cormier (2020) entry References. The Hefesto thermodynamic mineral code is available at the web link: https://github.com/stixrude/HeFESToRepository.

590 **References**

591 Andrews, J., & Deuss, A. (2008), Detailed nature of the 660 km region of the mantle from global
592 receiver function data. *J. Geophys. Res.*, 113 (B6). doi:10.1029/2007JB005111.
593
594 Blundell, S.J., & Blundell, K.M. (2014), Ch. 28 In: *Thermal Physics*, Oxford University Press,
595 Oxford, UK.
596
597 Burdick, L.J., & Helmberger, D.V. (1978), The upper mantle P velocity structure of the western
598 United States. *J. Geophys. Res.*, 83 (B4), 1699-1712.
599
600 Chu, R., Schmandt, B., & Helmberger, D.V. (2012), Upper mantle P velocity structure beneath
601 the midwestern US derived from triplicated waveforms, *Geochem. Geophys., Geosys.,* 13 (2), doi:
602 10.1029/2011GC003818.
603
604 Cormier, V.F., Tian, Y., & Zheng, Y. (2020), Heterogeneity spectrum of Earth's upper mantle
605 obtained from the coherence of teleseismic P waves. *Commun. Comp. Phys.*, 28, 74-97. doi:
606 10.4208/cicp.OA-2018-0079.
607
608 Deuss., A., Redfern, S.A.T., Chambers, K., & Woodhouse, J.H. (2006), The nature of the 660
609 km discontinuity in Earth's mantle from global seismic observations of PP precursors. *Science*,
610 311, 198-201.
611
612 Ekstrom, G., Nettles, M., & Dziewoski, A. M. (2012), The global CMT project 2004-2010:
613 Centroid moment tensors for 13,017 earthquakes. *Phys. Earth Planet. Int.,* 200-201, 1-9, doi:
614 10.1016/j.pepi.2012.04.002.
615
616 Evans, J.R. (1982), Running median filters and a general despiker, *Bull. Seism. Soc. Am.*, 72(1),
617 331-338.
618

619 Hao, S., Wang, W., Qian, W., & Wu, Z. (2019), Elasticity of akimotoite under the mantle
620 conditions: Implications for multiple discontinuities and seismic anisotropies at the depth ~600-
621 750 km in subduction zones. *Earth Planet. Sci. Lett.,* 528, 115830.
622
623 Hogrefe, A., Rubie, D.C., & Sharp, T.G. (1994), Metastability of enstatite in deep subducting
624 lithosphere. *Nature*, 372 351-353.
625
626 Hosseini, K., Matthews, K,J., Sigloch, K., Shepard, G.E., Domeier, M., & Tsekhmistrenko, M.
627 (2018), SubMachine: Web-based tools for exploring seismic tomography and other models of
628 Earth's deep interior, *Geochem., Geophys., and Geosys.*, 19(5), 1464-1483, doi:
629 10.1029/2018GC007431.
630
631 Karato, S. (1992), On the Lehmann discontinuity, *Geophys. Res. Lett.*, 19, 2255– 2258.
632
633 Ishii, T., Huang, T., Myhill, R., Fei, H. Koemets, L., Liu, Z., Maeda, F., Yuan, L., Wang, L.,
634 Druzhbin, D., Yamamoto, T., Bhat, S., Faria, R., Kawazoe, T., Tsujino, N., Kulik, E., Higo, Y,
635 Tange, Y., & Katsura, T. (2019), Sharp 660-km discontinuity controlled by extremely narrow
636 binary post-spinel transition. *Nature Geoscience*, 12, 869-872.
637
638 Klimes, K. (2002), Correlation functions of random media. *Pure Appl. Geophys.*, 159 1811-
639 1831.
640
641 Mao, W., & Zhong, S., (2008), Slab stagnation due to a reduced viscosity layer beneath the
642 mantle transition zone, *Nature Geosci.*, 11, 876-881.
643
644 Mancinelli, N., & Shearer, P., Liu, Q. (2016), Constraints on the heterogeneity spectrum of
645 Earth's upper mantle. *J. Geophys. Res.,* 121 (5), 3703-3721.
646
647 Matyska, C., & Yuen, D.A. (2002), Bullen's parameter eta: a link between seismology and
648 geodynamical modelling, Earth. *Planet. Sci. Lett.,* 198, 471-493.
649

650 Montagner, J.P., & Kennett, B.L.N. (1995), How to reconcile body-wave and normal-mode
651 reference Earth models? *Geophys. J. Int.*, 135-229-248.
652
653 Nissen-Meyer, T., van Driel, M., Stähler, S. C., Hosseini, K., Hempel, S., Auer, L., Colombi, A.,
654 & Fournier, A. (2014) AxiSEM: broadband 3-D seismic wavefields in axisymmetric media.
655 *Solid Earth*, 5, 425-445, https://doi.org/10.5194/se-5-425-2014.
656
657 Ono, S. (2007), The Lehmann discontinuity due to dehydration of subducted sediment, *The Open*
658 *Mineralogy Journal*, 1(1), 1-4, doi: 10.2174/1874456700801010001.
659
660 Pugh, S., Jenkins, J., Boyce, A., & Cottar, S. (2021) Global receiver function observations of the
661 X-discontinuity reveal recycled basalt beneath hotspots, *Earth Planet. Sci. Lett,* 561, doi:
662 10.1016/j.epsl.2021.116813.
663
664 Sato, H., Fehler, M.C., & Maeda, T. (2012)*, Seismic Wave Propagation and Scattering in the*
665 *Heterogeneous Earth,* 2nd edn., Springer-Verlag.
666
667 Schmid, C., Goes, S., van der Lee, S., & Giardini, D. (2002), Fate of the Cenozoic Farallon slab
668 from comparison of kinematic thermal modeling with tomographic images. *Earth and Planet.*
669 *Sci. Lett.,* 204, 17-32.
670
671 Shearer, P. (1991), Constraints on upper mantle discontinuities from observations of long-period
672 reflected and converted phases. *Journal of Geophysical Research*, 96(B11), 18,147– 18,182.
673
674 Simmons, N.A., S.C. Myers, G. Johannesson, & E. Matzel (2012), LLNL-G3Dv3: Global P-
675 wave tomography model for improved regional and teleseismic travel time prediction, *J.*
676 *Geophys. Res*., 117, doi:10.1029/2012JB009525.
677
678 Solomon, S.C. (1976), Geophysical constraints on radial and lateral temperature variations in the
679 upper mantle, *Am. Mineral.*, 61(7-8), 788-903.

Stixrude, L., & Lithgow-Bertelloni, C. (2007), Influence of phase transformations on lateral dynamics in Earth's mantle. *Earth Planet. Sci. Lett,* 263, 45-55.

Stixrude, L., & Lithgow-Bertelloni, C. (2012), Geophysics of chemical heterogeneity in the mantle. *Ann. Rev. Earth Planet. Sci*., 40, 569-595, doi: 10.1146/annurev.earth.36.031207.124244.

Stixrude, L., & Lithgow-Bertelloni, C. (2022), Thermal expansivity, heat capacity and bulk modulus of the mantle, *Geophys. J. Int.* , 228(2), 1119-1149, doi: 10.1093/gji/ggab394.

Tackley P.J., Stevenson, D. J., & Glatzmaier G.A. (1993), Effects of an endothermic phase transition at 670 km depth in a spherical model of convection in the Earth's mantle. *Nature* 361:699-704

Tian, Y., & Cormier, V.F., (2020), https://github.com/vernoncormier/stochastic_tomography, doi:/10.528/zenodo.4000538.

Tkalčić, H., Cormier, V.F., Kennett,B.L.N., & He, K. (2010), Steep reflections from the Earth's core reveal small-scale heterogeneity in the upper mantle. *Phys. Earth Planet. Int.*, 178, 80-91. doi: 10.1016/j.pepi.2009.08.004.

Vinnik, L., Kurnik, E., & Farra, V. (2005), Lehmann discontinuity beneath North America: No role for seismic anisotropy, *Geophys. Res. Lett.*, 32(9), doi: 10.1029/2004GL022333.

Vinnik, L., Kozlovskaya, E., Oreshin, S., & Kosarev, G. (2015), *Tectonophysics*, 667(23), 189-198, doi: 10.1016/tecto.2015.11.024.

Wessel, P., & Smith, W.H.F. (1998), New, improved version of the Generic Mapping Tools released, *Eos Trans. AGU*, 79, 579.

Whitcomb, J.H., & Anderson, D.L. (1970), Reflection of P'P' seismic waves from discontinuities in the mantle, *J. Geophys. Res.*, 75(29), 5713-5728.

Wu, R.S., & Flatté, S. (1990), Transmission fluctuations across an array and heterogeneities in the crust and upper mantle. *Pure Appl. Geophys.*, 132, 175-196.

Wu, R.S., & Xie, X. (1991), Numerical tests of stochastic tomography. *Phys. Earth Planet. Inter.*, 67 (1991) 180-193.

Xu, W., Lithgow-Bertelloni, C., Stixurde, L., & Ritsema, J. (2008), The effect of bulk composition and temperature on mantle seismic structure. *Earth. Planet. Sci. Lett.*, 275, 70-79.

Zhao, Y., Wu, Z., Wang, W., Deng, X., & Song, J. (2022), Elastic properties of Fe-bearing Akimotoite at mantle conditions: Implications for composition and temperature in the lower mantle transition zone, Fundamental Research, doi: 10.1016/j.fmre.2021.12.013.

Zheng, Y., & Wu, R.-S. (2008), Theory of transmission fluctuations in random media with a depth dependent background velocity structure. *Adv. Geophys.*, 50, 21-41.